Journal of Magnetic Resonance 303 (2019) 91–104

Contents lists available at ScienceDirect

Journal of Magnetic Resonance

journal homepage: www.elsevier.com/locate/jmr

# A spin-thermodynamic approach to characterize spin dynamics in TEMPO-based samples for dissolution DNP at 7 T field

Fabian Jähnig [a], Aaron Himmler [a], Grzegorz Kwiatkowski [b], Alexander Däpp [a], Andreas Hunkeler [a], Sebastian Kozerke [b], Matthias Ernst [a,*]

[a] Physical Chemistry, ETH Zürich, Vladimir-Prelog-Weg 2, 8093 Zürich, Switzerland
[b] Institute for Biomedical Engineering, University and ETH Zürich, Gloriastrasse 35, 8092 Zürich, Switzerland

ARTICLE INFO

*Article history:*
Received 7 January 2019
Revised 12 April 2019
Accepted 19 April 2019
Available online 25 April 2019

*Keywords:*
Dynamic nuclear polarization
Dissolution DNP
Spin thermodynamics

ABSTRACT

The spin dynamics of dissolution DNP samples consisting of 4.5 M [$^{13}$C]urea in a mixture of $(1/1)_{Vol}$ glycerol/water using 4-Oxo-TEMPO as a radical was investigated. We analyzed the DNP dynamics as function of radical concentration at 7 T and 3.4 T static magnetic field as well as function of deuteration of the solvent matrix at the high field. The spin dynamics could be reproduced in all cases, at least qualitatively, by a thermodynamic model based on spin temperatures of the nuclear Zeeman baths and an electron non-Zeeman (dipolar) bath. We find, however, that at high field (7 T) and low radical concentrations (25 mM) the nuclear spins do not reach the same spin temperature indicating a weak coupling of the two baths. At higher radical concentrations, as well as for all radical concentrations at low field (3.4 T), the two nuclear Zeeman baths reach the same spin temperature within experimental errors. Additionally, the spin system was prepared with different initial conditions. For these cases, the thermodynamic model was able to predict the time evolution of the system well. While the DNP profiles do not give clear indications to a specific polarization transfer mechanism, at high field (7 T) increased coupling is seen. The EPR line shapes cannot clarify this in absence of ELDOR type experiments, nevertheless DNP profiles and dynamics under frequency-modulated microwave irradiation illustrate the expected increase in coupling between electrons with increasing radical concentration.



## 1. Introduction

In dissolution dynamic nuclear polarization (DNP), microwave irradiation is used to transfer the large electron polarization to nearby nuclear spins at low temperatures with subsequent rapid dissolution of the sample using a hot solvent [1]. The possibility to generate highly-polarized solutions of small molecules, led to a renaissance of DNP in nuclear magnetic resonance (NMR) and magnetic resonance imaging (MRI) especially for nuclei with low gyromagnetic ratios. Applications have been developed in different areas like medical MRI and in-vivo spectroscopy [2–10], investigation of chemical processes using NMR [11–15], and material science [16–20].

Dissolution DNP experiments are carried out at low temperature (1–2 K) in dedicated polarizers often optimized for specific applications. Two main pathways to obtain high polarization of low gamma nuclei exist: either direct hyperpolarization of the low-gamma target nucleus or using hyperpolarization of $^{1}$H followed by Hartmann-Hahn cross polarization (CP) [21] to transfer the polarization to the target nuclei. Currently, the main application of dissolution DNP is the production of highly-polarized [1-$^{13}$C]-pyruvic acid for use in *in vivo* metabolic imaging. This is usually achieved using trityl radicals to directly enhance the $^{13}$C polarization in selectively labeled pyruvic acid. Due to the ready availability of micro-wave sources around 95 GHz (W band, 3.4 T static field), many of the first-generation polarizers were built at this frequency [1,22–24]. It was soon realized that the direct $^{13}$C DNP process profits from higher static magnetic fields, where higher polarization levels in the solid state could be achieved. Therefore, polarizers operating at higher static magnetic fields were developed first at 6.8–7 T and later using cryogen-free magnets with variable fields up to 10 T [25–29].

Using DNP to protons with subsequent cross polarization to low-gamma nuclei leads typically to a much faster polarization build up and requires samples doped with radicals that exhibit broad EPR lines, e.g., TEMPO derivatives, that allow efficient polarization of $^{1}$H. At lower magnetic fields (3.4 T) experimental results showed that different nuclei (e.g., proton and carbon) have the

* Corresponding author.
*E-mail address:* maer@ethz.ch (M. Ernst).

https://doi.org/10.1016/j.jmr.2019.04.012
1090-7807/

same enhancement factor and reach the same final spin temperature [30], a feature often associated with the thermal-mixing model [31–35]. In this case, a thermodynamic spin-temperature based model could be used to describe and predict the spin dynamics in such samples [30]. Such a description based on rate equations was also used to describe systems composed of pyruvic acid doped with trityl [36–38].

The use of a spin-thermodynamic description of the polarization-transfer dynamics is only loosely connected to the underlying physical model that leads to the DNP process. Whether the thermal-mixing model is indeed the mechanism of polarization transfer in such samples is still an open question. It was shown that a combination of cross-effect DNP and additional heteronuclear mixing can lead to similar effects in semi-analytical models of small spin systems [39,40]. Recent results show that the spin dynamics in such samples depend heavily on composition and measurement conditions, with the change in static magnetic field playing a major role [28,39,41–48]. But to the best of our knowledge none of the analytical models is able to predict optimum sample compositions useful in applications. Therefore, optimizing sample parameters including solvent matrix, radical concentration or concentration of the substrate to be polarized still needs experimental screening.

The availability of polarizers operating at higher frequencies raised the question how polarization transfer from electrons to nuclei in samples with TEMPO derivatives can be described at higher static magnetic fields. Recently published results at 6.8 T show that in samples doped with TEMPOL, thermal mixing also seems to be the dominant mechanism at higher magnetic fields [49]. In this publication, we present experimental data on DNP at 7 T using 4-Oxo-TEMPO at different radical concentrations. We compare the results to equivalent data acquired at 3.4 T. In addition, a spin-thermodynamic model is used to fit and predict the spin dynamics in these samples at different concentrations and for different initial conditions of the magnetization. We also investigate the influence of deuteration of the solvent matrix on the achievable polarization on the low gamma nuclei at lower fields and compare this to results obtained at 3.4 T [30,43]. To this end, different degrees of deuteration of the solvent have been used, with the consecutive measurements performed for all three nuclei ($^{1}$H, $^{2}$H and $^{13}$C).

To better understand the DNP process, it is important to understand the EPR properties of the samples as well as their NMR characteristics. Recently it became clear that understanding the EPR properties of the doping agent is necessary to unravel the processes in the samples under microwave irradiation [38,41,50]. This motivated the implementation of longitudinally detected EPR (LOD EPR) in our probe [22,51,52]. Despite being low-cost and simple in design, the technique, at least in principle, allows detection of important EPR parameters, e.g. $T_{1e}$, given sufficiently capable microwave generation.

## 2. Hardware and experiments

### 2.1. Polarizer and LOD setup

The polarizer used in this work was previously described in detail [53]. Addition of a Helmholtz coil to the static non-dissolution probe (see photograph in Fig. 1(b)) allows performing longitudinally-detected EPR (LOD EPR) experiments and was used to detect the EPR line shape of the radicals under DNP conditions. In LOD experiments the amplitude of the continuous-wave (CW) microwave field applied to the sample is modulated, periodically saturating the z-component of the electron magnetization. The periodic saturation induces a time-dependent voltage in the Helmholtz coil which can subsequently be detected either in a broadband fashion or using a lock-in amplifier set to the frequency of the modulation in the low kHz range.

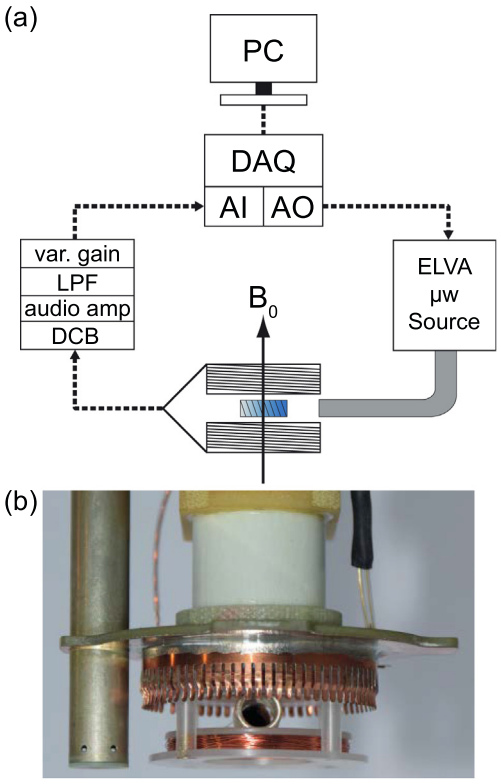


**Fig. 1.** (a) Schematic representation of the whole LOD setup including its amplifier stages, with a DC block (DCB) and a low-pass filter (LPF) and control setup via a NI DAQ connected to the PC controlling the whole polarizer setup. (b) Photograph of the LOD setup attached to the low end of the probe.

The design of this setup, schematically depicted in Fig. 1(a), follows previously published versions of LOD setups [22,51,52]. It uses a National Instruments data acquisition device (NI USB-6229 DAQ) to feed an analog waveform to the microwave source, while simultaneously acquiring the LOD EPR signal.

Our microwave source (Model VCOM-10/94/200-DD, ELVA-1) provides 50 mW of power between 196.8 and 197.8 GHz featuring a voltage-controlled power attenuator (0–40 dB). For LOD experiments the source is operated in CW mode with the waveform from the NI DAQ fed to its attenuator port modulating its amplitude at a frequency of up to 5 kHz. For the frequency-modulated data, a new microwave amplifier multiplier chain from Virginia Diodes (Charlotteville, VA, U.S.A.) with an output power of 140 mW was used. The frequency range of the VDI source is 10 GHz and frequency modulation schemes can be programmed directly on the microcontroller of the source.

The EPR detection circuit utilizes a broadband detection scheme and consists of the Helmholtz coil (100 µm wire, $2 \times 750$ turns) placed such that the sample holder sits in-between the two sections as shown in Fig. 1(a) and (b) such that the axis of the coil is parallel to the $B_0$ field. The Helmholtz coil is non-resonant (broadband) and well insulated from ground to avoid cross talk from the microwave signal. The coil is pseudo-differentially connected to an amplifier stack schematically shown in Fig. 1(a). The stack consists of a DC block (DCB), an audio preamplifier (SSM2019) followed by a 90 kHz low-pass filter (LPF) and finally a second gain stage with variable gain levels (79–119 dB). Overall the frequency range of this stack is 210 Hz to 28 kHz corresponding to the audible frequency range, which makes noise suppression very important. To this end small weights were attached to the waveguide going into

the probe to reduce vibrations. In addition, a directional coupler was used as a dampening weight at the top of the waveguide, such that the flexible WR05 waveguide connects two heavier parts (directional coupler on one, microwave source on the other side), further dampening the vibrations.

To achieve the best possible SNR all acquisition parameters were optimized experimentally. In general, a high number of averages (15000 averages were used in the experiments described here) per frequency step were needed to generate enough SNR. Correspondingly, amplitude modulation at 1 and 3.5 kHz frequency exhibited the highest SNR. The highest gain setting of 119 dB also led to the best SNR, albeit only for the mentioned high number of averages. Lowering the temperatures from 50 to 20 K improved the available SNR from roughly 5 to over 23. Reducing the temperature further did not result in additional improvement, but the achievable SNR stayed above 20, which is in general lower compared to other designs [22,51]. Nonetheless, the listed parameters enabled recording of the EPR line under DNP conditions with 51 steps over the whole frequency range, requiring approximately 15–20 min of measurement time. A small DC offset was also present, but could be corrected with a linear baseline correction.

### 2.2. Materials and sample preparation

All samples were prepared in a two-step process. First a stock solution of 4.5 M [$^{13}$C]urea (fully protonated, Sigma Aldrich, Buchs, Switzerland) in solvent mixtures of $(1/1)_{Vol}$ glycerol/water was prepared. Second, appropriate amounts of 4-Oxo-TEMPO (4-Oxo-2,2,6,6-tetramethyl-1-piperidinyloxy, Sigma Aldrich, Buchs, Switzerland) were weighed before mixing them with the stock solution to achieve doping levels of 25, 50 and 75 mM. In each case, 70 μL of sample was vortexed prior to loading it into the sample container. Filled containers were shock frozen in liquid nitrogen for ca. 30 s inside the NMR coil before inserting them into the polarizer to ensure reproducible glass formation. The sample container consists of a PTFE cylinder (3 mm inner diameter, 0.05 mm wall thickness) with 2 Kel-F end caps. Different degrees of deuteration were used for the solvent matrix as listed in detail in Table. 3.

### 2.3. DNP profiles and buildup/decay curves

All measurements were performed at 4.2 K due to the long experimental time available in this mode for our cryogenic setup [30,53]. The full measurement protocol consisted of thermal equilibrium, buildup and decay curves, LOD EPR and DNP profile measurements, during a single measurement session, without taking the sample out of the magnet.

DNP profiles correlate the microwave frequency with enhancement by stepping the microwave frequency through the frequency range of interest. In this work, a step size of 0.02 GHz was used, and a single enhancement measured using a saturation-recovery pulse sequence with a relaxation period of 60–180 s between saturation and acquisition, depending on sample and spin species. Four low flip-angle (2–4°), phase-cycled pulses were used to acquire each data point.

DNP buildup and decay of the polarization were measured in a single experiment, with an FID recorded every 60–120 s using four phase-cycled, low flip-angle (2–4°) pulses. In most of the experiments, 10 dB of attenuation had to be used before the receiver to accommodate the enhanced NMR signal within the range of the ADC. Additionally, a thermal equilibrium measurement was recorded for each newly filled sample container in order to calculate enhancements and absolute polarization levels. For the thermal-equilibrium measurements, 30–50 FIDs were recorded, with identical pulse settings as used for the buildup/decay curves, after an initial relaxation delay of 5 $T_1$. In between FIDs the relaxation delay was chosen such that the polarization could recover to roughly 99% of its equilibrium value, considering the saturation due to the measurement pulses. No attenuation but the same receiver-gain settings as for DNP buildups or profiles were used.

### 2.4. Probe background and data analysis

To ensure proper calculation of enhancement factors and absolute polarization levels, the probe background needs to be considered. Therefore, an empty sample container, which was prepared the same way as a normal sample (see Section 2.2), was inserted into the polarizer. Subsequently the signal of the empty sample container was acquired using identical acquisition parameters as in buildup/decay experiments. For $^{13}$C no background signal could be measured, but for $^{1}$H significant background could be recorded.

All data sets where processed using MATLAB (The Mathworks, Natick, MA, U.S.A.). The data were phased manually and subsequently zero filled by a factor of two, then Fourier transformed without any additional processing. To calculate the signal intensities the spectra were first baseline corrected (linear correction) and then numerically integrated. Due to the line shape resulting from the quadrupolar powder pattern fitting the $^{2}$H data was not possible with a single Voigt-type function, so the numerical integration was performed over the actual data. Subsequently, the integrated signal intensity was normalized to the integrated thermal signal corrected for the different attenuation in the receiver pathway used in the buildup measurements. The buildup and decay curves were fitted with a mono-exponential decay to obtain enhancements $\varepsilon$, buildup time constants $\tau$ and $T_1$ relaxation times, respectively.

### 2.5. Spin-thermodynamic model and fitting

The model used to describe the spin dynamics is based on spin thermodynamics and was presented in detail in a previous publication and given in the Supplemental Material [30]. A schematic of the model is shown in Fig. 2. It describes the transfer of magnetization between the three spin baths, i.e., carbon Zeeman (CZ), proton Zeeman (HZ), electron non-Zeeman (eNZ) and a cooling bath (CL), with three coupled differential equations including seven free parameters: $R_C$, $R_H$, $R_e$, $k_C$, $k_H$, $R_{CL}$ and $\varepsilon_{CL}$. Its main assumption about the EPR line is that its electron non-Zeeman part can be represented by a spin bath with the capacity of a spin-1/2 system whose energy levels are separated by the frequency corresponding to the width of the EPR line. This can only be valid if very fast spectral diffusion is present within the EPR line, which usually is only the case for strong electron-electron interaction. The validity of

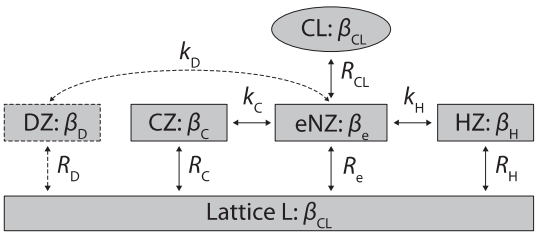


**Fig. 2.** Schematic representation of the spin-thermodynamic model used to fit experimental data. It shows the four spin baths (deuterium Zeeman (DZ), carbon Zeeman (CZ), proton Zeeman (HZ), and electron non-Zeeman bath (eNZ) the relaxation-rate constants ($R_X$) that connect the baths with the lattice and the rate constants ($k_X$) that connect the nuclear Zeeman baths with the electron non-Zeeman bath. The cooling bath (CL) is connected with the constant $R_{CL}$ with the eNZ bath. In this work, the deuterium Zeeman bath is not used leaving seven free parameters (see text for more details).

this assumption in the cases presented will be discussed at a later point.

To fit the model to each sample separately the heat capacities of the spin baths (protons, carbons, electrons) were calculated from their Curie constants, based on the respective molarity of each spin species within the given sample. Numerical solving of the differential equation and optimizing the given start parameters was implemented in MATLAB using its ODE solver and fminsearch algorithms, respectively. For each sample, four datasets, buildup and decay curves for both $^{1}H$ and $^{13}C$, were used to optimize the parameters in the system of differential equations. In order to fit the model, the cumulative norm of the differences between model predictions and data points was minimized starting from a randomly chosen set of seven start values for the model parameters. To reduce the chance of finding a local minimum, the optimization routine was run for 300 randomly chosen sets of start parameters, with each optimization running for a maximum of 1500 iterations. Additionally, parallelization was utilized increasing the speed of the calculation drastically, therefore, allowing multiple runs within a few hours.

Initial tests showed that the cooling bath temperature $\beta_{CL}$, as well as the cooling rate $R_{CL}$ did not influence the other fitting parameters as long as the cooling bath was colder than the lowest temperature of the spin baths, and $R_{CL}$ was fast enough to cool down the eNZ spin temperature. This is not surprising since the experimental data (nuclear spin temperatures) are only indirectly connected to these two values. Therefore, the cooling bath temperature $\beta_{CL}$, as well as the cooling rate $R_{CL}$ were fixed for the data evaluation. Reducing the number of free fit parameters from seven to five lead to better convergence, such that more than 3/4 of all starting sets resulted in parameters with an error norm of less than 5% worse than the best set. To allow higher enhancements, as found for the deuterated samples presented in Section 3.5, the cooling bath temperature $\beta_{CL}$ (or its enhancement) needed to be relaxed to a temperature lower than the lowest one experimentally measured (or its enhancement higher than the maximum measured). Accordingly, the cooling rate $R_{CL}$ needed adjustment to counteract this change such that the original data used to fit the model parameters was reproduced.

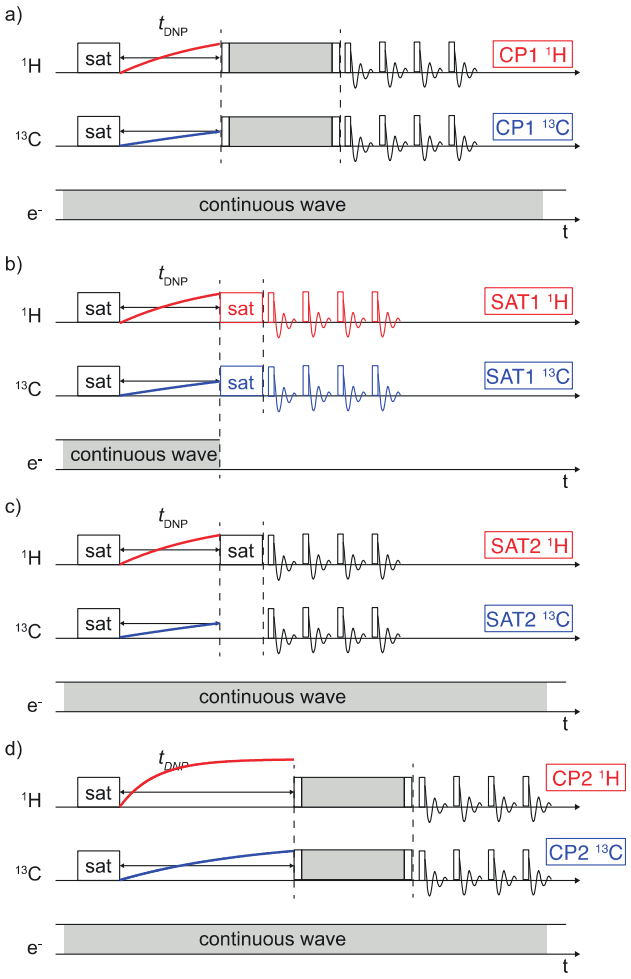


**Fig. 3.** Pulse sequence schematics for the four different initial conditions used to cross check the spin-thermodynamic model. In pulse sequences (a), (c) and (d) both channels are measured after the same preparation sequence. In (b) only the channel where the saturation occurs is measured.

### 2.6. Variation of spin-system initial conditions

To investigate the spin dynamics in select samples in more detail, the spin system was prepared in different initial conditions and the subsequent time evolution was recorded using continuous small flip angle acquisitions every 30–120 s.

In initial condition (i) (Fig. 3a) the time evolution of both spin species after a CP step from $^{1}H$ to $^{13}C$, i.e., after increasing the $^{13}C$ polarization beyond its equilibrium value, is measured while both polarizations are still building up under microwave irradiation, either after a DNP buildup time of 30 or 60 s. The micro-wave irradiation was kept on during the whole experiment.

The preparation of the initial condition (ii) (Fig. 3b) was the following: after reaching the DNP plateau, a saturation train was used on either $^{13}C$ or $^{1}H$ while simultaneously switching off the microwave irradiation. Afterwards the time evolution of the polarization of the saturated spin was measured, while the other spin was left to decay without interference.

Similarly, initial condition (iii) (Fig. 3c) uses a saturation train on $^{1}H$ during the DNP buildup, typically after either 180 or 60 s for sample B and C respectively, while measuring both spin polarizations after the saturation train but under continuous microwave irradiation.

In initial condition (iv) (Fig. 3d) again a CP step from $^{1}H$ to $^{13}C$ is used but in contrast to initial condition (i) after the $^{1}H$ have reached their DNP plateau value, typically after 120 to 360 s, before measuring both spin polarizations. The sample was irradiated with microwave during the whole experiment.

In total this amounts to four different preparations of the initial state of the spin system with different relative enhancement levels on the two spins. Two of them use a CP step to transfer polarization from protons to carbons (conditions (i) and (iv)), while the other two (ii) and (iii) use saturation pulses to zero the polarization of on spin species. Only in case number (ii) was the microwave source turned off during the measurement of the time evolution after the preparation of the initial condition while the other three use continuous microwave irradiation during the whole experiment.

### 2.7. Frequency-modulated microwave irradiation

Frequency modulation (FM) of the microwave irradiation can be programmed on the VDI source. A triangular frequency modulation with a variable bandwidth (0–250 MHz) around the center frequency and a modulation frequency of 500 Hz was used in all measurements. The modulation frequency was optimized experimentally on the 50 mM sample as well as the microwave power which was set to 50 mW unless indicated otherwise.

## 3. Results

### 3.1. EPR line shape and DNP profiles at different radical concentrations

The shape of the EPR line determines the corresponding nuclear DNP profile, which correlates the microwave frequency with the DNP enhancement. The two measurements contain important information about the DNP process, and ideally one wants to correlate them. Furthermore, they are also important to find optimum conditions in order to maximize the achievable polarization. In samples with water-based solvent matrices these profiles and the EPR line shape depend crucially on the concentration of the radical, since it governs the possible aggregation of the radical within the glassy sample. Fig. 4 shows the normalized profiles and EPR line of three samples using different concentrations of 4-oxo-TEMPO at 7 T field.

In sample A (25 mM 4-oxo-TEMPO) the EPR line is dominated by the g-factor anisotropy of the nitroxide radical as seen in Fig. 4(a) (black dashed line). Its $^{13}$C profile (blue) exhibits similar features as the EPR line on the low-frequency side (hyperfine coupling to $^{14}$N) while the proton profile only shows features at the very low-frequency end of the profile. Both nuclei show a slight asymmetry in the profile, as the high-frequency minimum enhancement is slightly lower than the low-frequency maximum enhancement. For $^{13}$C the maximum is at 197.18 GHz, while the minimum is at 197.38 GHz, resulting in a frequency difference of $\Delta f$ = 200 MHz. For $^{1}$H (Fig. 4(a), red line) the minimum is at the same position but the maximum is at 197.1 GHz, which results in a difference of $\Delta f$ = 280 MHz.

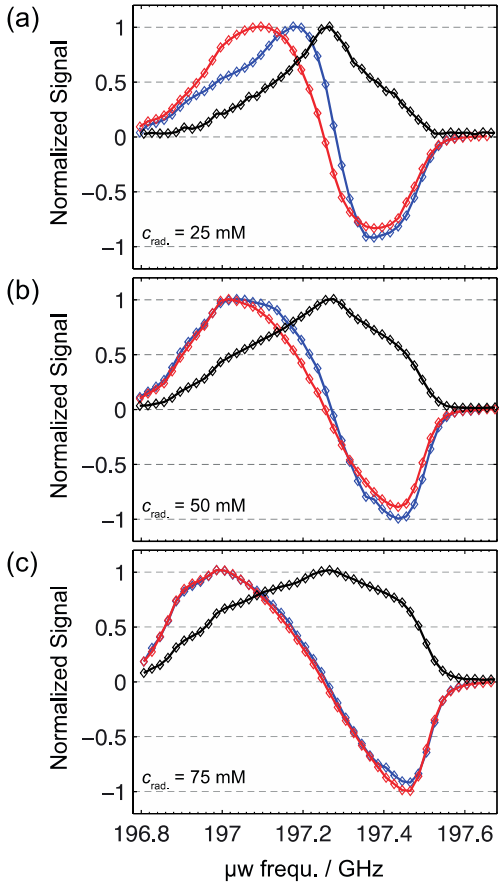


**Fig. 4.** Normalized DNP profiles for $^{1}$H (red) and $^{13}$C (blue) as well as the EPR line (black) recorded using the LOD technique for: (a) sample A with 25 mM, (b) sample B with 50 mM and (c) sample C with 75 mM of 4oxo-TEMPO recorded at 7 T field. Profiles and EPR extend below 196.8 GHz, which is the limit of our microwave equipment. Individual data points are marked by a small diamond. (For interpretation of the references to colour in this figure legend, the reader is referred to the web version of this article.)

Sample B (50 mM 4oxo-TEMPO, Fig. 4(b)) shows significantly more broadening in the EPR line shape, which is likely a result of the increased electron-electron interaction, i.e., the EPR line is broadened in addition to the g-anisotropy. As a result, the hyperfine coupling to $^{14}$N, which is well visible in Fig. 4(a), is more obscured in Fig. 4(b). In this case the $^{13}$C DNP profile maximum moves closer to the $^{1}$H maximum and lies at 197.04 GHz, while the $^{13}$C minimum is at 197.44 GHz, giving $\Delta f$ = 400 MHz. Protons show a very similar DNP profile with the maximum at 197.02 GHz, while the profile minimum is at 197.44 GHz as for $^{13}$C. This corresponds to a difference of $\Delta f$ = 420 MHz.

In Fig. 4(c) data for sample C (75 mM 4oxo-TEMPO) shows an even stronger broadened EPR line, compared to Fig. 4(b) and (a). Interestingly the hyperfine coupling to $^{14}$N seem to be better visible than in (b). Correspondingly, some of these features are also reflected in the DNP profiles of $^{1}$H and $^{13}$C, whose profiles coincide in this case. Their maximum enhancement at 197.00 GHz and their minimum enhancement at 197.47 GHz leads to a difference of $\Delta f$ = 470 MHz.

At 3.4 T field the profiles for both nuclei coincide at all radical concentrations investigated. The frequency difference between the maximum enhancements for both $^{1}$H and $^{13}$C increases from $\Delta f$ = 300 MHz at 25 mM radical to $\Delta f$ = 350 MHz at a radical concentration of 50 and 75 mM as shown in the Supporting Material Fig. S1. The difference between the samples is significantly less pronounced at 3.4 T compared to 7 T, but broadening of the profiles is clearly visible, leading to a loss of small features in the profiles (compare Fig. S1).

### 3.2. Buildup-decay curves for different radical concentrations

The buildup and the decay of $^{1}$H and $^{13}$C polarization under microwave irradiation was investigated for the three samples A, B and C (see Section 3.1) with radical concentrations of 25, 50, and 75 mM, respectively. Fig. 5 shows the buildup (left column) and decay curves (right column) of protons (red squares) and carbons (blue circles), while the shaded area represent one standard deviation from multiple experimental runs with separate freezing of the sample. While in sample A (Fig. 5(a), 25 mM radical) the maximum enhancement for protons of 45.4 is about a factor of two lower than for carbons at 84.4, it is almost within the error for sample B with $\varepsilon$ = 101.7/108.4 for $^{13}$C/$^{1}$H respectively (Fig. 5(b), 50 mM radical) and converges at $\varepsilon$ = 98.7/97.9 for sample C (Fig. 5(c), 75 mM radical). Buildup times $\tau$ and decay times $T_1$ get shorter with increased radical concentration, as exemplified by the difference in timescale on the x-axes of Fig. 5(a)–(c). Buildup-times and $T_1$ reduce roughly by a factor of three in between samples A and B and a factor two for the second concentration step (B to C). A summary of the values of all three parameters extracted using mono-exponential fits to the curves in Fig. 5 is given in Table 1 (left half).

The same experiments at a lower static magnetic field of 3.4 T are shown in Fig. 6. The resulting buildup (left column) and decay (right column) curves for protons (red squares) and carbon (blue circles) were measured in the same samples (A to C). All DNP parameters extracted by mono-exponential fits are summarized in Table. 1 (right half). In contrast to the previously presented results at 7 T, at the lower field no clear regime change with radical concentration is observed. Although $^{1}$H enhancements increase slightly from 45.6 to 55.1/58.3 from 25 mM to 50/75 mM radical concentration, all three samples (A, B and C) exhibit a $^{13}$C enhancement close to $\varepsilon$($^{1}$H), with 49, 68.1 and 62.3. Simultaneously both

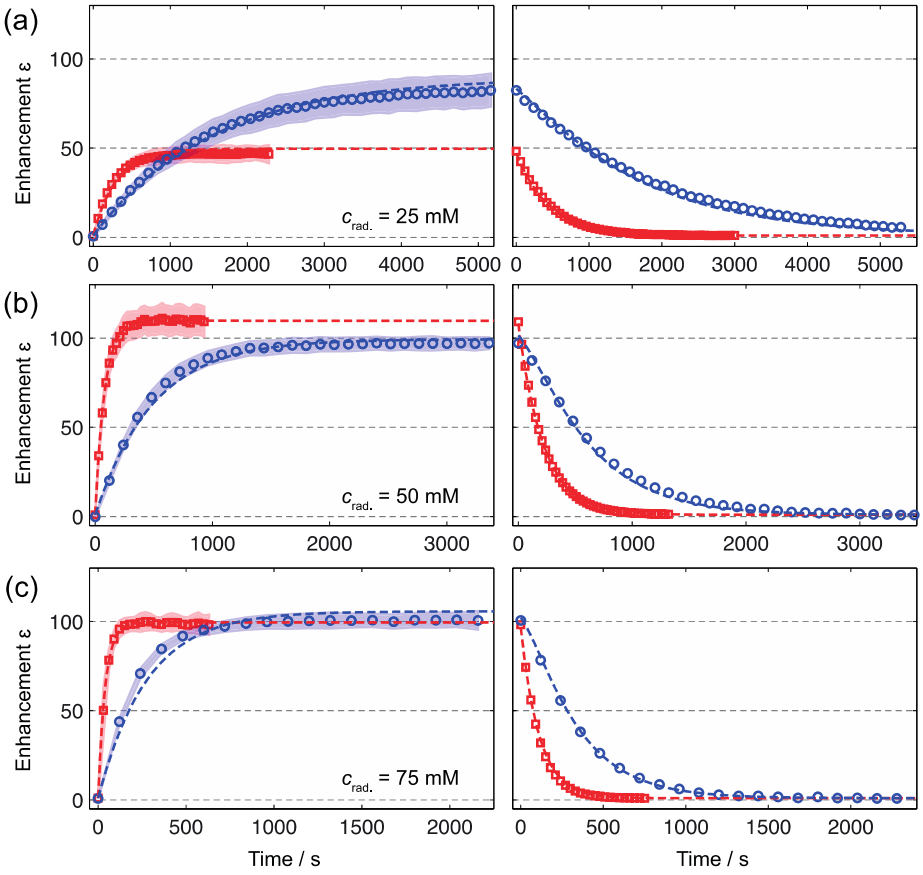


**Fig. 5.** Buildup (left column) and decay (right column) curves for protons (red squares) and carbons (blue circles) for three different radical concentrations: (a) 25 mM, (b) 50 mM and (c) 75 mM measured at 7 T field. Shaded background areas indicate the error from different experimental runs with separate vitrifying of the sample. For the decays the error lies within the plotted symbols and is left out for clarity. Dashed lines represent the fits of the spin-thermodynamic model introduced in Section 2.5. (For interpretation of the references to colour in this figure legend, the reader is referred to the web version of this article.)

**Table 1**
Summarized DNP parameters extracted from mono-exponential fits to data at 7 T (left half) and 3.4 T (right half).

| Sample | 7 T | | | | | | 3.4 T | | | | | |
|---|---|---|---|---|---|---|---|---|---|---|---|---|
| | $^{13}$C | | | $^{1}$H | | | $^{13}$C | | | $^{1}$H | | |
| | A | B | C | A | B | C | A | B | C | A | B | C |
| $\varepsilon$ | 84.4 | 101.7 | 98.7 | 45.4 | 108.4 | 97.9 | 49 | 68.1 | 62.3 | 45.6 | 58.3 | 55 |
| $\tau$ / s | 1271 | 414 | 205 | 242 | 81 | 39 | 346 | 117 | 57 | 102 | 34 | 18 |
| $T_1$ / s | 1850 | 666 | 349 | 439 | 216 | 106 | 420 | 169 | 91 | 192 | 82 | 42 |

time constants decrease with increasing amounts of radical present in the sample by the same factors as at higher field (3 from sample A to B and 2 from B to C) but the absolute timescales are much faster at 3.4 T. Comparing these data to previously published results with TEMPOL based samples at the lower field (3.4 T), it is clear that the results are almost identical [30].

In addition to the mono-exponential fits, we also used the spin-thermodynamic model presented in Section 2.5 to extract the time constants from the data. Fitting the buildup and decay data simultaneously the parameters presented in Table 2 (top half) reproduce the data very well, even for the case of sample A (25 mM) where both spin species do not exhibit the same enhancement, i.e., spin temperature, which indicates weak thermal contact.

Taking a closer look at the parameters in Table. 2 we see that the rates with which $^{13}$C ($R_C$) and $^{1}$H ($R_H$) relax increase with increasing radical concentration at both magnetic fields (compare top and bottom). The same is true for the coupling of either nuclear bath to the electron non-Zeeman bath, which also increases from sample A to C, e.g. from 0.46 via 3.9–7.07 $s^{-1}$ for $^{1}$H at 7 T field (top half), and similarly for $^{13}$C although at a much slower timescale. At 3.4 T field the increase in coupling for $^{1}$H is only present going from sample A to B, from ca. 5–20 $s^{-1}$, albeit less pronounced (only by a factor four instead of eight at 7 T). Afterwards the coupling does not further increase for $^{1}$H. For $^{13}$C the coupling also shows a drastic increase at first, from 0.0024–0.0091 $s^{-1}$, and a smaller increase to 0.014 $s^{-1}$ at the second concentration step.

Comparing the parameters from these model fits it is clear that they reflect the changes in the time constants ($T_1$ and $\tau$) between 3.4 T and 7 T also seen in the mono-exponential fits shown in Table 1. Simultaneously, a much lower coupling between the baths is found at 7 T, especially for protons, although the ratio between the two coupling constants $k_C$ and $k_H$ stays comparable when going to higher field. Interestingly the parameters for the virtual cooling reservoir change significantly between 3.4 and 7 T. At the higher field cooling needs to be stronger (higher rate $R_{CL}$) and the cooling-baths temperature needs to be colder (higher enhancement

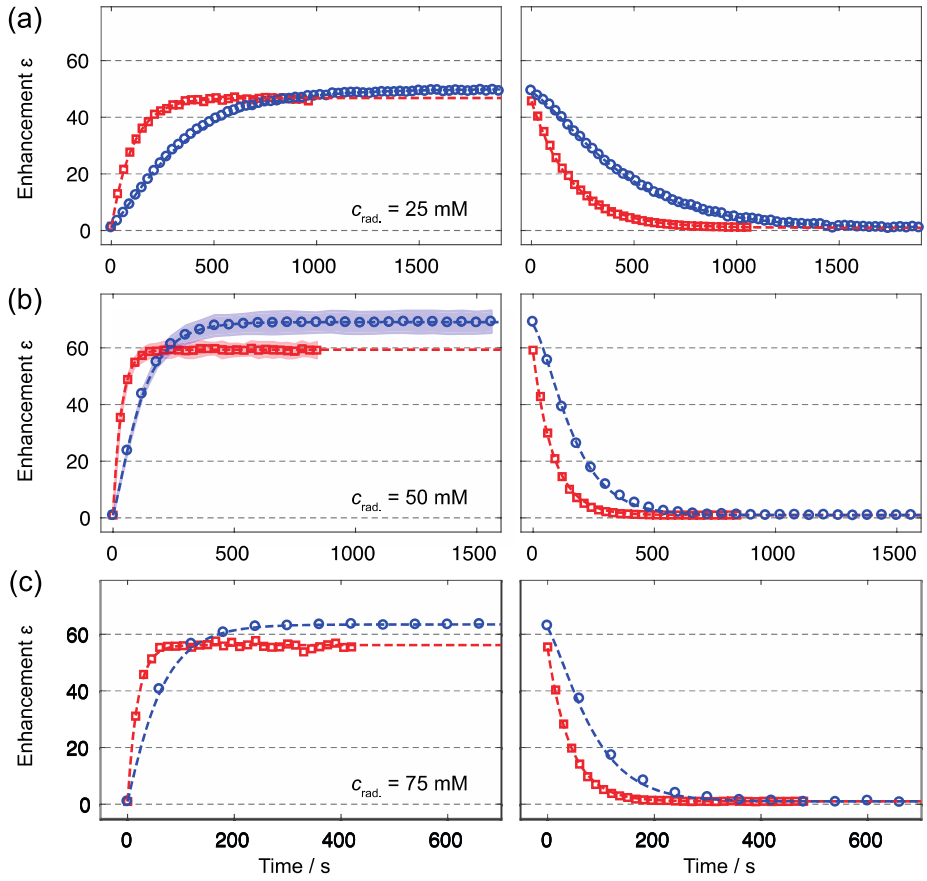


**Fig. 6.** Buildup (left column) and decay (right column) curves for protons (red squares) and carbons (blue circles) for three different radical concentrations: (a) 25 mM, (b) 50 mM and (c) 75 mM measured at 3.4 T field. Shaded background areas in panel (b) indicate the error from different experimental runs with separate freezing of the sample. (For interpretation of the references to colour in this figure legend, the reader is referred to the web version of this article.)

**Table 2**
Parameters for the spin-thermodynamic model at 7 T (top) and 3.4 T field (bottom, see text for details).

| Sample | $R_C$ [$s^{-1}$] | $R_H$ [$s^{-1}$] | $R_e$ [$s^{-1}$] | $k_C$ [$s^{-1}$] | $k_H$ [$s^{-1}$] | $R_{CL}$ [$s^{-1}$] | $\varepsilon_{CL}$ |
|---|---|---|---|---|---|---|---|
| A | $2.62\ 10^{-4}$ | $2.25\ 10^{-3}$ | $1.6\ 10^{-4}$ | $3.88\ 10^{-4}$ | 0.46 | 250 | 150 |
| B | $6.74\ 10^{-4}$ | $3.31\ 10^{-3}$ | $5.88\ 10^{-1}$ | $1.37\ 10^{-3}$ | 3.9 | 100 | 150 |
| C | $1.05\ 10^{-3}$ | $8.4\ 10^{-3}$ | $1.2\ 10^{-1}$ | $2.57\ 10^{-3}$ | 7.07 | 100 | 150 |
| A | $8.23\ 10^{-4}$ | $5.1\ 10^{-3}$ | $1.2\ 10^{-5}$ | $2.4\ 10^{-3}$ | 4.98 | 7.9 | 100 |
| B | $5.88\ 10^{-4}$ | $1.2\ 10^{-2}$ | $4.93\ 10^{-5}$ | $9.1\ 10^{-3}$ | 20.4 | 14.7 | 100 |
| C | $4.1\ 10^{-3}$ | $2.4\ 10^{-2}$ | $6.3\ 10^{-3}$ | $1.4\ 10^{-2}$ | 20.81 | 27.4 | 100 |

$\varepsilon_{CL}$) in order to fit the model to the data. But this fact should not be overemphasized, since these two parameters work together with $R_e$ to determine the enhancement of the electron non-Zeeman bath and are, therefore, only indirectly determined by the experimental data. With that in mind the model could in principle be simplified to contain fewer parameters, which is what we implemented by fixing $R_{CL}$ and $\varepsilon_{CL}$.

Overall, the decrease in coupling within the model fits and the difference in cooling reservoir parameters hints at the fact that the physics of the polarization transfer changes significantly when increasing the radical concentration and also when going from 3.4 to 7 T field strength.

### 3.3. Spin-system initial conditions and model predictions

For the two samples B and C, which show, in the quasi-equilibrium state under microwave irradiation, the same spin temperature for carbons and protons within the experimental errors, the response of the system to different initial conditions was measured to assess how well the spin-thermodynamic model can predict the spin dynamics in different situations. These initial conditions are described in detail in Section 2.6 and include two with a cross-polarization (CP) step (initial condition (i) and (iv)) and two with saturation of one or both nuclei (initial condition (ii) and (iii)). The experimental data are shown in Fig. 7 for sample B (50 mM TEMPO) and in Fig. 8 for sample C (75 mM TEMPO).

Figs. 7 and 8 show that the model predicts the time evolution for all initial conditions well. Especially the time evolution of the protons is captured almost perfectly while there are some deviations for the carbon time evolution.

Starting from initial conditions (ii) and (iv) the agreement between experiments and model predictions is almost perfect for both samples (see Figs. 7 and 8(b) and (d)). Less well predicted are the time evolution for starting initial conditions (i) and (iii) corresponding to the data in Fig. 7(a) and (c). There are two main discrepancies between the thermodynamic model and experimental data. For one the model does not describe the buildup dynamic

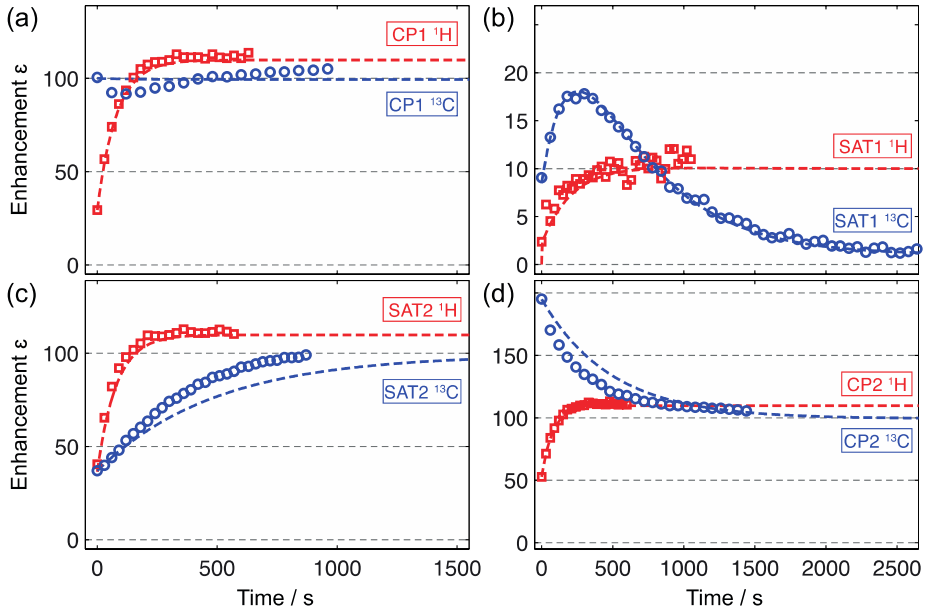


**Fig. 7.** Evolution of the enhancements of $^{1}$H (red squares) and $^{13}$C (blue circles) during four different initial conditions: (a) equals initial condition (i), (b) initial condition (ii), (c) initial condition (iii) and (d) initial condition (iv) (see text for detailed explanation of initial condition) recorded for sample B (50 mM 4oxo-TEMPO). Dashed lines show respective predictions from the spin thermodynamic model mentioned in the text. Proton enhancement in panel (b) is increased by a factor ten for visibility. (For interpretation of the references to colour in this figure legend, the reader is referred to the web version of this article.)

accurately. In both cases the model predicts a slower buildup of the enhancement albeit the final plateau value is predicted very well in all cases. The only exception is Fig. 7(a), showing initial condition (i) for sample C, where the experimental data is clearly lower than the model prediction. But the experimental enhancement is also lower than the enhancement measured previously for the standard buildup-curves (see Fig. 5(c)). We suspect that there was either an issue with sample heating or other experimental errors that lead to lower final polarization values. A final answer to this would require multiple measurements of each of the initial conditions.

Another feature that is no very well reproduced is the initial mixing behavior of the carbon bath after a saturation of the protons (initial condition i), as can be seen in Fig. 7(a) and to a minor extend also in Fig. 8(a).

### 3.4. Frequency-modulated microwave irradiation

It has been shown that dissolution DNP samples using radicals with broad EPR lines show higher enhancements when modulating the frequency of the microwave field [54–56]. Modulating the microwave frequency within a 250 MHz band around a center frequency with a modulation frequency of 500 Hz (see Section 2.7 for details) resulted in notably different results for the samples A, B and C as shown in Fig. 9.

Sample A (25 mM TEMPO) shows a significant boost in enhancement and a reduction in the buildup time for both proton and carbon spins. Proton enhancement is increased from 43 to 80 corresponding to an increase by a factor of almost 2. At the same time the buildup time decreases moderately from 290 s to 220 s. The data also shows that a smaller modulation band width (100 MHz) leads to only slightly lower values than the maximum modulation bandwidth. For carbon the enhancement in polarization is similar going from 85 to 150 corresponding to an increase by a factor 1.8 and the buildup time decreasing from 1530 s to 1250 s (Fig. 9(d)). Despite the very different DNP profiles (see Fig. 4(a)), the frequency modulation of the microwave irradiation has very similar effects on the achievable enhancement and the buildup time of both spins.

Increasing the radical concentration to 50 mM (sample B) leads to a more modest improvement for protons from 90 to 100, while the buildup time is almost constant changing from 45 s to 42 s. For $^{13}$C we also find a slightly higher enhancement, increasing from 90 to 120, while the buildup time is reduced less than 10%, namely 470 s compared to 435 s. However, the proton enhancement shows a shallow maximum around 100 MHz modulation bandwith and the carbon enhancement levels off already at 50 MHz.

Raising the concentration of 4-oxo-TEMPO even further, to 75 mM, (sample C) leads to a regime change, where frequency modulation has a mostly negative effect on the DNP performance as can be seen from Fig. 9(c) and (f). In the case of $^{1}$H the enhancement reduces from 97 to 80 for the full modulation of 200 MHz. Only a very small modulation bandwidth of 50 MHz gives slightly higher enhancements. At the same time the buildup time remains roughly the same at 34 s. For $^{13}$C we see a similar picture with a drop of the enhancement from 87 to 83 and a slight rise in buildup time from 215 s to 223 s.

All data discussed so far were acquired with a microwave power of 50 mW which was experimentally optimized for the 50 mM sample. In addition, we have also measured one data point using the maximum available power of 110 mW at the maximum modulation bandwidth of 250 MHz. One can clearly see a boost of the achievable polarization at higher microwave power which is accompanied by a further reduction in build-up times.

Because frequency-modulated microwave irradiation covers a broader part of the EPR line than standard cw irradiation it should also change the DNP profile if it is recorded using FM, since it averages enhancements at multiple frequencies along the DNP profile within the modulation band used, in line with the previous reports for $^{1}$H earlier [54]. To check if this hypothesis also holds for $^{13}$C, a DNP profile was recorded for sample A (Fig. 10). It uses a coarser step size of 0.05 GHz for the microwave frequency and modulation width of $\Delta f = 100$ MHz around this center frequency. Indeed, the shape changes significantly, as expected when using

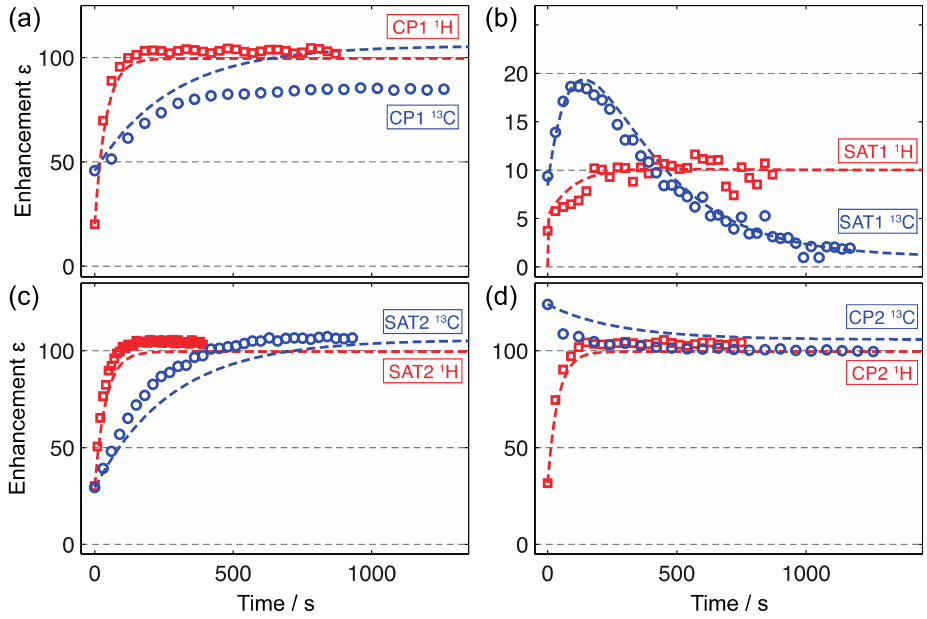


**Fig. 8.** Dynamics of enhancements of $^{1}$H (red squares) and $^{13}$C (blue circles) in sample C (75 mM 4oxo-TEMPO) for four different initial conditions: (a) equals initial condition (i), (b) initial condition (ii), (c) initial condition (iii) and (d) initial condition (iv) (see text for detailed explanation of scenarios). Dashed lines show respective predictions from the spin thermodynamic model presented in Section 2.5. Proton enhancement in panel (b) is increased by a factor ten for visibility. (For interpretation of the references to colour in this figure legend, the reader is referred to the web version of this article.)

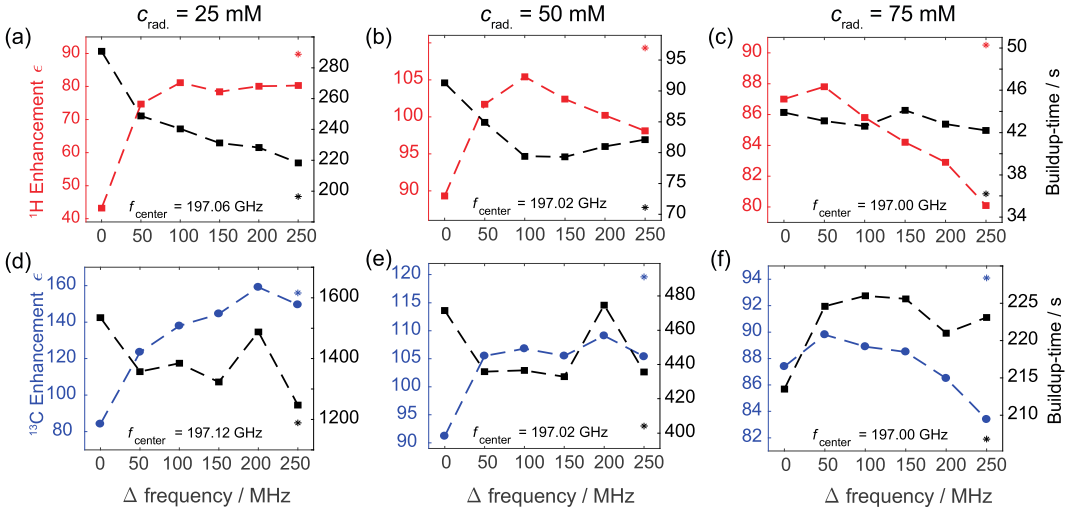


**Fig. 9.** Enhancements of $^{1}$H (red squares) and $^{13}$C (blue circles) and buildup-times τ (black squares) achieved with frequency-modulated microwave irradiation. Δ frequency refers to range of modulation of the Microwave frequency while $f_{center}$ gives the center frequency of the modulation range. A zero modulation range stands for non-modulated cw microwave irradiation. Modulation was achieved programming the VDI source to generate a triangular frequency modulation with a modulation frequency of 500 Hz. (a)/(d) refer to sample A (25 mM radical), (b)/(e) to sample B (50 mM radical) and (c)/(f) to sample C (75 mM radical). The microwave power was 50 mW except for the data points indicated by * where it was set to the maximum power of 110 mW. (For interpretation of the references to colour in this figure legend, the reader is referred to the web version of this article.)

frequency-modulated microwave irradiation (dashed, light blue line Fig. 10) compared to standard cw irradiation (Fig. 10 blue line, red diamonds). The wings of the profile are more pronounced than without modulation and also the position of the minimum changes towards higher frequencies, namely 197.45 GHz.

### 3.5. Effect of deuteration of solvent matrix on spin dynamics

Different degrees of deuteration were applied to sample B (50 mM radical), see Table 3, in order to study the effect on the spin dynamics. All samples contain 4.5 M [$^{13}$C] urea, which causes the difference between solvent and sample deuteration. Our setup also allowed measuring $^{2}$H data to include into the analysis.

Changing the solvents deuteration degree has no significant effect on the DNP profiles of all participating nuclei. Data is shown in the Supplemental Material in Fig. S2.

Buildup and decay dynamics of samples B, B1 and B2 are plotted in Fig. 11(a)–(c) in the left and right column respectively. All samples show an increase in enhancement with increasing degree of deuteration going from around 100 without deuteration to 200 when fully deuterated with an intermediate step of 150 for sample B1. While $^{1}$H and $^{2}$H show very similar enhancements in samples B1 and B2, the enhancement of $^{13}$C also increases but to a lower

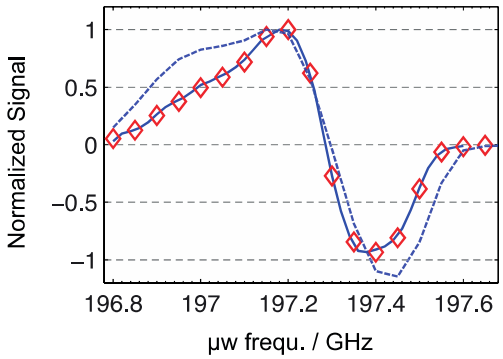


**Fig. 10.** Normalized $^{13}C$ DNP profile for sample A (25 mM radical) without microwave frequency modulation (blue line), with frequency modulated microwave irradiation (dashed blue line) and with coarse steps in microwave frequency without modulation (red diamonds). (For interpretation of the references to colour in this figure legend, the reader is referred to the web version of this article.)

**Table 3**
Deuteration degrees of the solvent matrix used for samples doped with 50 mM 4-Oxo-TEMPO.

| Sample | Solvent deuteration | Sample deuteration | Solvent $(1/1)_{vol}$ |
|---|---|---|---|
| B | 0% | 0% | Glycerol/$H_2O$ |
| B1 | 50% | 58% | Glycerol-d3/$D_2O$ |
| B2 | 100% | 85% | Glycerol-d8/$D_2O$ |

degree, which increases the difference between $^{13}C$ on the one side and $^{1}H/^{2}H$ on the other.

In terms of buildup time we see a shortening for $^{1}H$ from 81 s to around 31–33 s, while $^{13}C$ and $^{2}H$ do not show a conclusive trend towards shorter buildup times, with $\tau$ being shortest for the intermediate case B1 and increasing again for sample B2. A similar situation is found for the decay times $T_1$ where protons also exhibit shorter times at higher deuteration degree while carbon and deuterium do not show a conclusive trend towards any direction. See Table 4 for a full summary of the parameters.

Dashed lines in Fig. 11 show the predictions from the spin-thermodynamic model, each colored according to the nuclear species, red for $^{1}H$, blue for $^{13}C$. The decay dynamics are predicted very well for zero deuteration (sample B, panel (a)) and full deuteration (sample B2, panel (c)), but not completely for the intermediate case (sample B1, panel (b)). Buildup times are predicted well, except for $^{13}C$ in sample B1 where the buildup is slightly underestimated. The increase in enhancement is captured by the model for all three samples with a slight overestimation for $^{1}H$ in sample B1 and a slight underestimation for $^{13}C$ in sample B2. Keeping in mind that the error in these enhancements is about the same as for the buildup data shown in Fig. 5 the model prediction is still quite good.

## 4. Discussion

Recent theoretical analysis aiming to distinguish contributions from different DNP effects (solid effect, cross effect, thermal mixing) focused on an analysis of DNP profiles, rather than the spin dynamics in the time domain. Taking advantage of characteristic frequency differences between negative and positive DNP enhancements (e.g. $\sim 2\omega_N$ for the well-resolved solid effect), such an analysis compares the changes in DNP profiles at different temperatures (usually 5–50 K) using small scale quantum mechanical models [39,40,57]. However, in the experimental setup used here, such an approach is not possible due to technical limitations, therefore, we focused on an analysis of time-dependent spin dynamics. The data presented in Fig. 4 show that in none of the samples investigated a clear indication for a dominant DNP mechanism is given. The closest match is in sample A (25 mM 4-Oxo-TEMPO) where the frequency difference between enhancement maxima is 280 MHz, which is close to the proton Larmor frequency at 7 T which usually indicates a form of cross effect to be dominant. All other profiles show differences between extrema of 400–470 MHz, which does not correspond to a characteristic frequency difference for either nucleus. Clearly the two spins couple stronger when the concentration of the radical is increased. This is reflected in their respective DNP profiles (Fig. 4) which go from DNP profiles that are quite different at 25 mM to virtually identical ones at 75 mM radical concentration. At the same time, the enhancements also equilibrate to the same level for higher concentration of electrons, as seen in Fig. 5. These changes observed as a function of radical concentration hint at a change in DNP process. Yet the presented NMR data does not allow to unambiguously conclude which process is dominating.

In contrast to this, the data at 3.4 T shows no significant changes in the DNP profiles of $^{1}H$ and $^{13}C$, only additional broadening with increasing radical concentration is present. At this field the frequency difference between the enhancement maxima, which lies between 300 and 350 MHz, does not allow a clear statement of a DNP process, although for $^{1}H$ the frequency difference at 25 mM radical concentration indicates a form of cross effect. Similarly, the steady-state enhancements for both nuclei coincide for all three samples indicating a stronger coupling between the two nuclei already at lower radical concentrations. A small increase in steady-state enhancement is observed when increasing the radical concentration above 50 mM.

In principle, additional EPR measurements (under DNP conditions) might be able to further clarify the question of the mechanism underlying the observed DNP enhancement. While it is evident that homogeneous broadening due to increased electron-electron interaction is present if the concentration of 4-Oxo-TEMPO increases (see Fig. 4, black dashed lines) our setup does not allow ELDOR-type experiments to verify the amount of electron spin diffusion (eSD) as a function of the concentration. The electron relaxation time $T_{1e}$ cannot be measured with the employed microwave source, although it should in principle be possible with LOD EPR. Since it is, at the moment, also impossible to perform hole-burning experiments to assess saturation of the EPR line, our only indication toward eSD is the samples behavior under frequency-modulated microwave irradiation. In sample A with low radical concentration (see Fig. 9), both spins benefit significantly from sweeping the frequency, indicating that a bigger portion of the EPR line is saturated compared to standard cw irradiation. On the other hand, the enhancement of both spins in sample C, with a high radical concentration, drops with frequency modulation, indicating either an over- or under-saturation of the EPR line. Further studies are required to differentiate between the two cases and would require a full power-dependent study of the enhancement as a function of the modulation bandwidth. At low concentration, the coupling of the electrons is weaker but, interestingly, a spin-thermodynamic model can still fit the simultaneous polarization build up as shown in Fig. 5.

For samples B and C, the EPR line shape (broadening), the equilibration of DNP profiles and DNP enhancements, as well as the behavior under frequency-modulated microwave irradiation indicate that a spin thermodynamic model can be applied to describe the data. Fitting such a model (described in Section 2.5) to the buildup/decay data allowed us to reproduce the measured dynamics in these samples very well. Furthermore, the model is able to predict the spin dynamics in both samples for four different initial conditions, as shown in Figs. 7 and 8. This is an important cross check to confirm that the thermodynamic model characterizes

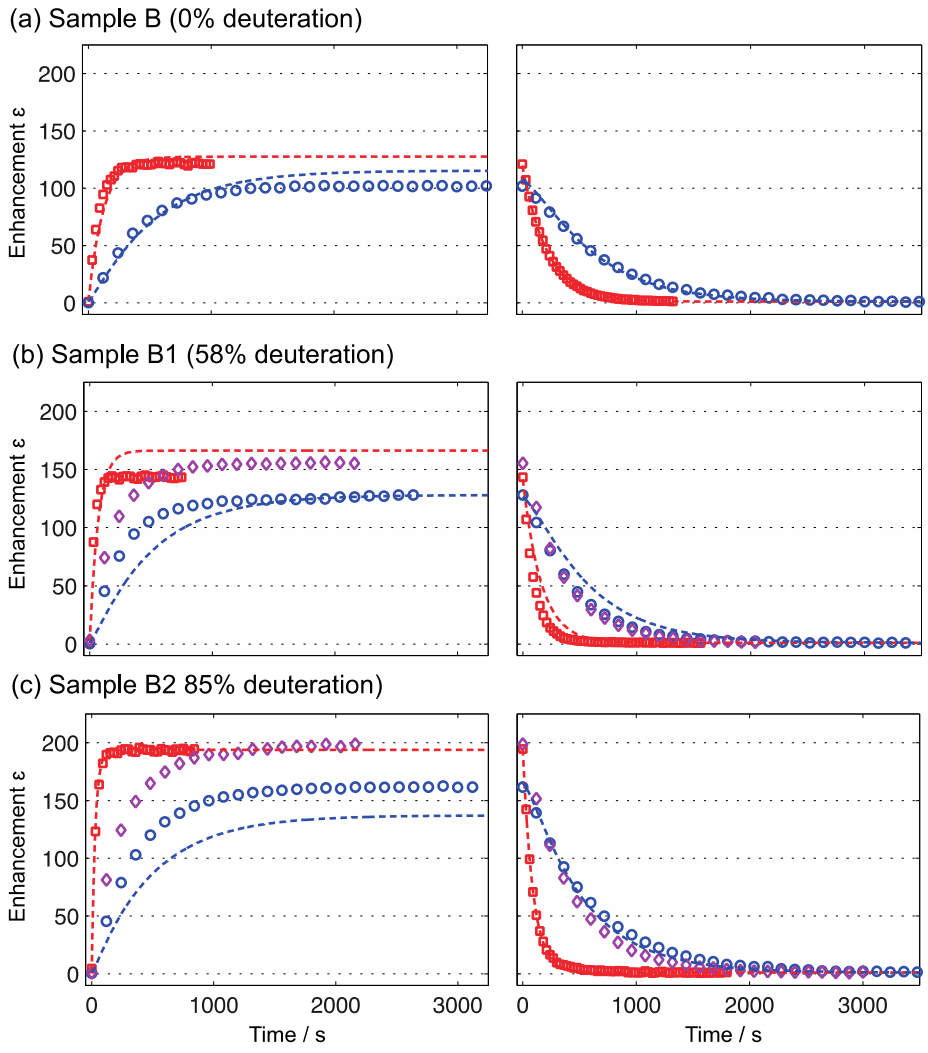


**Fig. 11.** Buildup (left column) and decay (right column) curves for $^{1}$H (red squares), $^{13}$C (blue circles) and $^{2}$H (magenta diamonds) in: (a) sample B, (b) sample B1 and (c) sample B2. Dashed lines in corresponding colors indicate predictions given the initial enhancement values and sample parameters but with adjusted cooling parameters in the model (for details see text). (For interpretation of the references to colour in this figure legend, the reader is referred to the web version of this article.)

**Table 4**
Summary of DNP fit parameters for samples B (fully protonated), B1 (58% deuterated) and B2 (85% deuterated) at 7 T field.

| Sample | $^{13}$C | | | $^{1}$H | | | $^{2}$H | | |
|---|---|---|---|---|---|---|---|---|---|
| | B | B1 | B2 | B | B1 | B2 | B | B1 | B2 |
| $\varepsilon$ | 108.1 | 126.8 | 165 | 119.9 | 141.5 | 183.5 | – | 154.1 | 194.4 |
| $\tau$/s | 395 | 268 | 361 | 81 | 33 | 31 | – | 203 | 251 |
| $T_1$/s | 662 | 438 | 597 | 218 | 100 | 91 | – | 361 | 413 |

the spin dynamics under various starting conditions and not only the polarization buildup that was used to fit the model. Since only experimental data of the nuclei are used to characterize the thermodynamic model, it is clear that the electron side of the model is not very well characterized. The outcome of the fits is quite insensitive to the heat capacity of the eNZ bath and the coupling to the cooling by microwave irradiation. The spin-thermodynamic model does not allow definite statements about the underlying quantum-mechanical processes that lead to the polarization transfer. But it might offer a simple way to predict how changes in the sample composition will influence the DNP polarization buildup.

The deuteration of the solvent matrix is often used to boost achievable polarization values. For deuterated samples, the DNP profiles of all involved nuclei do not change significantly as the degree of deuteration increases (shown in the Supplemental Material Fig. S2(a) to (c)). The achievable enhancements increase from roughly 100 at full protonation to around 200 at full deuteration of the solvent, as shown in Fig. 11. While $^{13}$C and $^{2}$H show similar timescales in their buildup and decay dynamics, they do not exhibit a conclusive trend with the degree of deuteration. Protons show a trend towards clearly shorter buildup/decay times with increasing deuteration degree and dynamics are in general much faster than either $^{13}$C or $^{2}$H. Since the concentration of electrons is constant within this set of samples and replacing $^{1}$H with $^{2}$H decreases the heat capacity of coupled systems as pointed out in the literature [58–60] this should lead to higher enhancements and faster build-up times. At the same time, the spin-diffusion process could

also be affected by the change in proton density leading to a potential slow-down of the polarization buildup. Experimentally, the polarization buildup accelerates with increased deuteration which is correctly predicted by the spin-thermodynamic model. At the same time, deuteration of either the labeled target molecule or the radical is beneficial due to increased $T_1$ times [61,62].

The prediction of the spin dynamics by our model for the deuterated samples works reasonably well by adjusting the molarity of the baths (Fig. 11, dashed lines). Compared to the fits of the fully protonated samples, the enhancement of the cooling bath had to be increased to 220 (from 150, see also Section 2.5 for details), and the cooling rate had to be decreased to $R_{CL} = 3.5\ s^{-1}$. With these changes, the original data could be reproduced, while also leading to a good prediction of the increased enhancements with increased deuteration of the solvent. The fact that the cooling rate becomes very small in order to balance the very cold temperature of the cooling bath is intuitive but highlights again that the properties of the electron spin bath within the spin-thermodynamic model are not very well defined by the experimental data.

To improve the model further, more EPR experiments under DNP conditions are necessary to ensure $R_{CL}$ and $\varepsilon_{CL}$ can be determined. The rest of the parameters can then be fit using the buildup/decay data as input. These show how the spin reservoirs are coupled for a given sample and indicate leakage of polarization to the lattice. Certainly, the model cannot predict the changes with radical concentration at the moment, although it even seems to work if the nuclear baths are not at the same temperature, which usually contraindicates the use of a thermodynamic description. More understanding of how the EPR parameters are affected by a change in radical concentration is necessary to explain this fact. Such detailed information might come from a quantum-mechanical approach to calculate interactions in the EPR line. Combining the two approaches, it might be possible to simulate how enhancements and timings change with sample composition.

## 5. Conclusion

In this article we presented experimental data on spin dynamics under static DNP conditions at 3.4 and 7 T field for samples composed of a glycerol/$H_2O$ matrix containing 4.5 M [$^{13}$C]urea doped with 4-Oxo-Tempo.

We compared the DNP profiles as well as the buildup and decay dynamics of the nuclear enhancement between the different field strengths for three different samples doped with increasing amounts of radical and discussed the experimental data within a spin-thermodynamic framework. While the DNP profiles were very similar for $^1$H and $^{13}$C for all samples measured at 3.4 T, we found a clear dependence on radical concentration measuring at 7 T, with increasing mixing of the two spins with increasing concentration. Similarly, we found a clear change in dynamics depending on radical concentration at 7 T field, namely an equilibration of the enhancements of both spins, which was not as strong at 3.4 T. In both cases the spin-thermodynamic model was able to characterize the dynamics well. At 7 T field we additionally used the model to predict the spin dynamics after four different initial state preparations and found that the predictions agree well with the experimental results. The spin dynamics can be fitted by a spin-thermodynamic model even in cases where the final spin temperatures of the nuclei do not reach the same level. This clearly shows that a spin-thermodynamic description is possible even in situations where the coupling of the two nuclear Zeeman baths is not very strong. It is currently unclear under which conditions such a model can successfully describe the spin dynamics.

We also investigated the impact of frequency-modulated microwave irradiation on the samples at 7 T field. Using frequency modulated microwave radiation, we found the same regime change with radical concentration as seen in the dynamics data. Low concentration samples (25 mM 4-Oxo-Tempo) benefit significantly from frequency modulation, while higher concentrations either do not benefit (sample B, 50 mM radical) or even show a drop in DNP enhancements with frequency modulation (sample C, 75 mM radical). We interpret this as a sign for increased coupling between electrons and increased electronic spin diffusion within samples with higher radical concentrations leading to under- or oversaturation of the EPR line.

Finally, we investigated how deuteration of the solvent matrix changes the dynamics within sample B at 7 T field. In general, all spins, including $^2$H, showed increased enhancements with increasing degree of deuteration, enhancements go from around 100 at full protonation to roughly 200 at full deuteration. At the same time only $^1$H exhibited a clear trend towards faster buildup and decay times, while the other spins showed no conclusive trend. After adjusting the cooling bath temperature, to allow enhancements of up to 220, and a corresponding change in the cooling rate $R_{CL}$, the spin-thermodynamic model was able to predict the increase in enhancements and shortening of the $^1$H time constants well, albeit with some error for $^{13}$C dynamics.

## Acknowledgements

We would like to thank Beat H. Meier for useful discussions. Financial support by the Swiss National Science Foundation (SNF grants 200021_149707 and 200020_169879) are gratefully acknowledged.

## Appendix A. Supplementary material

Supplementary data to this article can be found online at https://doi.org/10.1016/j.jmr.2019.04.012.

## References

[1] J.H. Ardenkjaer-Larsen, B. Fridlund, A. Gram, G. Hansson, L. Hansson, M.H. Lerche, R. Servin, M. Thaning, K. Golman, Increase in signal-to-noise ratio of > 10,000 times in liquid-state NMR, Proc. Natl. Acad. Sci. U.S.A. 100 (2003) 10158–10163, https://doi.org/10.1073/pnas.1733835100.
[2] K. Weiss, A. Sigfridsson, L. Wissmann, J. Busch, M. Batel, M. Krajewski, M. Ernst, S. Kozerke, Accelerating hyperpolarized metabolic imaging of the heart by exploiting spatiotemporal correlations, NMR Biomed. 26 (2013) 1380–1386, https://doi.org/10.1002/nbm.2963.
[3] P. Wespi, J. Steinhauser, G. Kwiatkowski, S. Kozerke, High-resolution hyperpolarized metabolic imaging of the rat heart using k–t PCA and k–t SPARSE, NMR Biomed. 31 (2018) 1–11, https://doi.org/10.1002/nbm.3876.
[4] J. Steinhauser, P. Wespi, G. Kwiatkowski, S. Kozerke, Assessing the influence of isoflurane anesthesia on cardiac metabolism using hyperpolarized [1- $^{13}$C] pyruvate, NMR Biomed. (2017) e3856, https://doi.org/10.1002/nbm.3856.
[5] T. Harris, H. Degani, L. Frydman, Hyperpolarized 13C NMR studies of glucose metabolism in living breast cancer cell cultures, NMR Biomed. 26 (2013) 1831–1843, https://doi.org/10.1002/nbm.3024.
[6] P. Dzien, A. Fages, G. Jona, K.M. Brindle, M. Schwaiger, L. Frydman, Following metabolism in living microorganisms by hyperpolarized 1H NMR, J. Am. Chem. Soc. 138 (2016) 12278–12286, https://doi.org/10.1021/jacs.6b07483.
[7] J.A.M. Bastiaansen, H.A.I. Yoshihara, A. Capozzi, J. Schwitter, R. Gruetter, M.E. Merritt, A. Comment, Probing cardiac metabolism by hyperpolarized $^{13}$C MR using an exclusively endogenous substrate mixture and photo-induced nonpersistent radicals, Magn. Reson. Med. 79 (2018) 2451–2459, https://doi.org/10.1002/mrm.27122.
[8] K.W. Lipsø, E.S.S. Hansen, R.S. Tougaard, C. Laustsen, J.H. Ardenkjær-Larsen, Dynamic coronary MR angiography in a pig model with hyperpolarized water, Magn. Reson. Med. 80 (2018) 1165–1169, https://doi.org/10.1002/mrm.27088.
[9] O.J. Rider, D.J. Tyler, Clinical implications of cardiac hyperpolarized magnetic resonance imaging, J. Cardiovasc. Magn. Reson. 15 (2013) 1–9, https://doi.org/10.1186/1532-429X-15-93.
[10] J. Kurhanewicz, D.B. Vigneron, J.H. Ardenkjaer-Larsen, J.A. Bankson, K. Brindle, C.H. Cunningham, F.A. Gallagher, K.R. Keshari, A. Kjaer, C. Laustsen, D.A. Mankoff, M.E. Merritt, S.J. Nelson, J.M. Pauly, P. Lee, S. Ronen, D.J. Tyler, S.S. Rajan, D.M. Spielman, L. Wald, X. Zhang, C.R. Malloy, R. Rizi, Hyperpolarized $^{13}$C MRI: path to clinical translation in oncology, Neoplasia (United States). 21 (2019) 1–16, https://doi.org/10.1016/j.neo.2018.09.006.

[11] Y. Kim, M. Liu, C. Hilty, Parallelized ligand screening using dissolution dynamic nuclear polarization, Anal. Chem. 88 (2016) 11178–11183, https://doi.org/10.1021/acs.analchem.6b03382.

[12] M. Liu, Y. Kim, C. Hilty, Characterization of chemical exchange using relaxation dispersion of hyperpolarized nuclear spins, Anal. Chem. 89 (2017) 9154–9158, https://doi.org/10.1021/acs.analchem.7b01896.

[13] M.H. Lerche, D. Yigit, A.B. Frahm, J.H. Ardenkjær-Larsen, R.M. Malinowski, P.R. Jensen, Stable isotope-resolved analysis with quantitative dissolution dynamic nuclear polarization, Anal. Chem. 90 (2018) 674–678, https://doi.org/10.1021/acs.analchem.7b02779.

[14] D. Kurzbach, E. Canet, A.G. Flamm, A. Jhajharia, E.M.M. Weber, R. Konrat, G. Bodenhausen, Investigation of intrinsically disordered proteins through exchange with hyperpolarized water, Angew. Chemie Int. Ed. 56 (2017) 389–392, https://doi.org/10.1002/anie.201608903.

[15] E. Monteagudo, A. Virgili, T. Parella, M. Pérez-Trujillo, Chiral recognition by dissolution DNP NMR spectroscopy of $^{13}$C-labeled dl-methionine, Anal. Chem. 89 (2017) 4939–4944, https://doi.org/10.1021/acs.analchem.7b00156.

[16] L. Piveteau, T.-C. Ong, A.J. Rossini, L. Emsley, C. Copéret, M.V. Kovalenko, Structure of colloidal quantum dots from dynamic nuclear polarization surface enhanced NMR spectroscopy, J. Am. Chem. Soc. 137 (2015) 13964–13971, https://doi.org/10.1021/jacs.5b09248.

[17] S. Björgvinsdóttir, B.J. Walder, A.C. Pinon, L. Emsley, Bulk nuclear hyperpolarization of inorganic solids by relay from the surface, J. Am. Chem. Soc. 140 (2018) 7946–7951, https://doi.org/10.1021/jacs.8b03883.

[18] K. Jeong, A.J. Parker, R.H. Page, A. Pines, C.C. Vassiliou, J.P. King, Understanding the magnetic resonance spectrum of nitrogen vacancy centers in an ensemble of randomly oriented nanodiamonds, J. Phys. Chem. C. 121 (2017) 21057–21061, https://doi.org/10.1021/acs.jpcc.7b07247.

[19] J. Järvinen, D. Zvezdov, J. Ahokas, S. Sheludyakov, O. Vainio, L. Lehtonen, S. Vasiliev, Y. Fujii, S. Mitsudo, T. Mizusaki, M. Gwak, S. Lee, S. Lee, L. Vlasenko, Microscopic control of Si-29 nuclear spins near phosphorus donors in silicon, Phys. Rev. B - Condens. Matter Mater. Phys. 92 (2015) 2–5, https://doi.org/10.1103/PhysRevB.92.121202.

[20] A. Lesage, M. Lelli, D. Gajan, M.A. Caporini, V. Vitzthum, P. Miéville, J. Alauzun, A. Roussey, C. Thieuleux, A. Mehdi, G. Bodenhausen, C. Copéret, L. Emsley, Surface enhanced NMR spectroscopy by dynamic nuclear polarization, J. Am. Chem. Soc. 132 (2010) 15459–15461, https://doi.org/10.1021/ja104771z.

[21] S.R. Hartmann, E.L. Hahn, Nuclear double resonance in the rotating frame, Phys. Rev. 128 (1962) 2042–2053, https://doi.org/10.1103/PhysRev. 128.2042.

[22] M. Batel, M. Krajewski, K. Weiss, O. With, A. Däpp, A. Hunkeler, M. Gimersky, K. P. Pruessmann, P. Boesiger, B.H. Meier, S. Kozerke, M. Ernst, A multi-sample 94 GHz dissolution dynamic-nuclear-polarization system, J. Magn. Reson. 214 (2012) 166–174, https://doi.org/10.1016/j.jmr.2011.11.002.

[23] A. Comment, B. Van Den Brandt, K. Uffmann, F. Kurdzesau, S. Jannin, J.A. Konter, P. Hautle, W.T. Wenckebach, R. Gruetter, J.J. van der Klink, Design and performance of a DNP prepolarizer coupled to a rodent MRI scanner, Concepts Magn. Reson. Part B Magn. Reson. Eng. 31B (2007) 255–269, https://doi.org/10.1002/cmr.b.20099.

[24] A. Feintuch, D. Shimon, Y. Hovav, D. Banerjee, I. Kaminker, Y. Lipkin, K. Zibzener, B. Epel, S. Vega, D. Goldfarb, A dynamic nuclear polarization spectrometer at 95 GHz/144 MHz with EPR and NMR excitation and detection capabilities, J. Magn. Reson. 209 (2011) 136–141, https://doi.org/10.1016/j.jmr.2010.12.010.

[25] A. Kiswandhi, P. Niedbalski, C. Parish, Q. Wang, L. Lumata, Assembly and performance of a 6.4 T cryogen-free dynamic nuclear polarization system, Magn. Reson. Chem. (2017) 1–7, https://doi.org/10.1002/mrc.4624.

[26] T.A. Siaw, A. Leavesley, A. Lund, I. Kaminker, S. Han, A versatile and modular quasi optics-based 200 GHz dual dynamic nuclear polarization and electron paramagnetic resonance instrument, J. Magn. Reson. 264 (2016) 131–153, https://doi.org/10.1016/j.jmr.2015.12.012.

[27] S. Jannin, A. Bornet, R. Melzi, G. Bodenhausen, High field dynamic nuclear polarization at 6.7 T: carbon-13 polarization above 70% within 20 min, Chem. Phys. Lett. 549 (2012) 99–102, https://doi.org/10.1016/j.cplett.2012.08.017.

[28] J.H. Ardenkjær-Larsen, S. Bowen, J.R. Petersen, O. Rybalko, M. Vinding, M. Ullisch, N.C. Nielsen, Cryogen-free dissolution dynamic nuclear polarization polarizer operating at 3.35 T, 6.70 T and 10.1 T, Magn. Reson. Med. 81 (2019) 2184–2194, https://doi.org/10.1002/mrm.27537.

[29] M. Baudin, B. Vuichoud, A. Bornet, G. Bodenhausen, S. Jannin, A cryogen-consumption-free system for dynamic nuclear polarization at 9.4 T, J. Magn. Reson. 294 (2018) 115–121, https://doi.org/10.1016/j.jmr.2018.07.001.

[30] M. Batel, A. Däpp, A. Hunkeler, B.H. Meier, S. Kozerke, M. Ernst, Cross-polarization for dissolution dynamic nuclear polarization, Phys. Chem. Chem. Phys. 16 (2014) 21407–21416, https://doi.org/10.1039/c4cp02696a.

[31] B.N. Provotorov, Magnetic resonance saturation in crystals, J. Exptl. Theor. Phys. 14 (1962) 1582–1591, https://doi.org/10.1590/S0102-311X1997000400023.

[32] A. Abragam, M. Goldman, Principles of dynamic nuclear polarisation, Rep. Prog. Phys. 41 (1978) 395–467, https://doi.org/10.1088/0034-4885/41/3/002.

[33] W.T. Wenckebach, Dynamic nuclear polarization via thermal mixing: Beyond the high temperature approximation, J. Magn. Reson. 277 (2017) 68–78, https://doi.org/10.1016/j.jmr.2017.01.020.

[34] W. de Boer, Dynamic orientation of nuclei at low temperatures, J. Low Temp. Phys. 22 (1976) 185–212, https://doi.org/10.1007/BF00655221.

[35] M. Borghini, Spin-temperature model of nuclear dynamic polarization using free radicals, Phys. Rev. Lett. 20 (1968) 419–421, https://doi.org/10.1103/PhysRevLett. 20.419.

[36] M. Filibian, S.C. Serra, M. Moscardini, A. Rosso, F. Tedoldi, P. Carretta, The role of the glassy dynamics and thermal mixing in the dynamic nuclear polarization and relaxation mechanisms of pyruvic acid, Phys. Chem. Chem. Phys. Phys. Chem. Chem. Phys. 16 (2014) 27025–27036, https://doi.org/10.1039/c4cp02636e.

[37] S.C. Serra, A. Rosso, F. Tedoldi, On the role of electron–nucleus contact and microwave saturation in thermal mixing DNP, Phys. Chem. Chem. Phys. 15 (2013) 8416–8428, https://doi.org/10.1039/C3CP44667K.

[38] S.C. Serra, A. Rosso, F. Tedoldi, Electron and nuclear spin dynamics in the thermal mixing model of dynamic nuclear polarization, Phys. Chem. Chem. Phys. 14 (2012) 13299, https://doi.org/10.1039/c2cp41947e.

[39] I. Kaminker, D. Shimon, Y. Hovav, A. Feintuch, S. Vega, Heteronuclear DNP of protons and deuterons with TEMPOL, Phys. Chem. Chem. Phys. 18 (2016) 11017–11041, https://doi.org/10.1039/c5cp06689a.

[40] D. Shimon, Y. Hovav, I. Kaminker, A. Feintuch, D. Goldfarb, S. Vega, Simultaneous DNP enhancements of $^{1}$H and $^{13}$C nuclei: theory and experiments, Phys. Chem. Chem. Phys. 17 (2015) 11868–11883, https://doi.org/10.1039/c5cp00406c.

[41] A. Leavesley, D. Shimon, T.A. Siaw, A. Feintuch, D. Goldfarb, S. Vega, I. Kaminker, S. Han, Effect of electron spectral diffusion on static dynamic nuclear polarization at 7 Tesla, Phys. Chem. Chem. Phys. 19 (2017) 3596–3605, https://doi.org/10.1039/c6cp06893f.

[42] A. Leavesley, C.B. Wilson, M. Sherwin, S. Han, Effect of water/glycerol polymorphism on dynamic nuclear polarization, Phys. Chem. Chem. Phys. 20 (2018) 9897–9903, https://doi.org/10.1039/c8cp00358k.

[43] P. Niedbalski, C. Parish, Q. Wang, A. Kiswandhi, L. Lumata, $^{13}$C dynamic nuclear polarization using derivatives of TEMPO free radical, Appl. Magn. Reson. 48 (2017) 933–942, https://doi.org/10.1007/s00723-017-0916-7.

[44] P. Niedbalski, C. Parish, Q. Wang, Z. Hayati, L. Song, A.F. Martins, A.D. Sherry, L. Lumata, Transition metal doping reveals link between electron $T_1$ reduction and $^{13}$C dynamic nuclear polarization efficiency, J. Phys. Chem. A. (2017), https://doi.org/10.1021/acs.jpca.7b09448, acs.jpca.7b09448.

[45] N. Enkin, G. Liu, I. Tkach, M. Bennati, High DNP efficiency of TEMPONE radicals in liquid toluene at low concentrations, Phys. Chem. Chem. Phys. 16 (2014) 8795–8800, https://doi.org/10.1039/c4cp00854e.

[46] D. David Jebaraj, H. Utsumi, A. Milton Franklin, Benial, dynamic nuclear polarization studies on deuterated nitroxyl spin probes, Magn. Reson. Chem. 55 (2017) 909–916, https://doi.org/10.1002/mrc.4602.

[47] L.L. Lumata, M.E. Merritt, C.R. Malloy, A.D. Sherry, Z. Kovacs, Impact of $Gd^{3+}$ on DNP of [1-$^{13}$C]Pyruvate Doped with Trityl OX063, BDPA, or 4-Oxo-TEMPO, J. Chem. Phys. A. 116 (2012) 5129–5138, https://doi.org/10.1021/jp302399f.

[48] P. Niedbalski, C. Parish, A. Kiswandhi, Z. Kovacs, L. Lumata, In fluence of $^{13}$C isotopic labeling location on dynamic nuclear polarization of acetate, J. Phys. Chem. A. 121 (2017) 3227–13223, https://doi.org/10.1021/acs.jpca.7b01844.

[49] D. Guarin, S. Marhabaie, A. Rosso, D. Abergel, G. Bodenhausen, K.L. Ivanov, D. Kurzbach, Characterizing thermal mixing dynamic nuclear polarization via cross-talk between spin reservoirs, J. Phys. Chem. Lett. 8 (2017) 5531–5536, https://doi.org/10.1021/acs.jpclett.7b02233.

[50] E.M.M. Weber, H. Vezin, J.G. Kempf, G. Bodenhausen, D. Abergél, D. Kurzbach, Anisotropic longitudinal electronic relaxation affects DNP at cryogenic temperatures, Phys. Chem. Chem. Phys. 19 (2017) 16087–16094, https://doi.org/10.1039/c7cp03242k.

[51] J. Granwehr, J. Leggett, W. Köckenberger, A low-cost implementation of EPR detection in a dissolution DNP setup, J. Magn. Reson. 187 (2007) 266–276, https://doi.org/10.1016/j.jmr.2007.05.011.

[52] A.J.P. Linde, A. Bornet, J. Milani, B. Vuichoud, R. Melzi, S. Jannin, G. Bodenhausen, Cross polarization from $^{1}$H to quadrupolar $^{6}$Li nuclei for dissolution DNP, Phys. Chem. Chem. Phys. 16 (2014) 24813–24817, https://doi.org/10.1039/C4CP03592E.

[53] F. Jähnig, G. Kwiatkowski, A. Däpp, A. Hunkeler, B.H. Meier, S. Kozerke, M. Ernst, Dissolution DNP using trityl radicals at 7 T field, Phys. Chem. Chem. Phys. 19 (2017) 19196–19204, https://doi.org/10.1039/c7cp03633g.

[54] A. Bornet, J. Milani, B. Vuichoud, A.J. Perez Linde, G. Bodenhausen, S. Jannin, Microwave frequency modulation to enhance dissolution dynamic nuclear polarization, Chem. Phys. Lett. 602 (2014) 63–67, https://doi.org/10.1016/j.cplett.2014.04.013.

[55] Y. Hovav, A. Feintuch, S. Vega, D. Goldfarb, Dynamic nuclear polarization using frequency modulation at 3.34 T, J. Magn. Reson. 238 (2014) 94–105, https://doi.org/10.1016/j.jmr.2013.10.025.

[56] I. Kaminker, S. Han, Amplification of dynamic nuclear polarization at 200 GHz by arbitrary pulse shaping of the electron spin saturation profile, J. Phys. Chem. Lett. 9 (2018) 3110–3115, https://doi.org/10.1021/acs.jpclett.8b01413.

[57] Y. Hovav, D. Shimon, I. Kaminker, A. Feintuch, D. Goldfarb, S. Vega, Effects of the electron polarization on dynamic nuclear polarization in solids, Phys. Chem. Chem. Phys. 17 (2015) 6053–6065, https://doi.org/10.1039/C4CP05625F.

[58] L. Lumata, M.E. Merritt, Z. Kovacs, Influence of deuteration in the glassing matrix on$^{13}$C dynamic nuclear polarization, Phys. Chem. Chem. Phys. 15 (2013) 7032–7035, https://doi.org/10.1039/c3cp50750e.

[59] A. Kiswandhi, B. Lama, P. Niedbalski, M. Goderya, J. Long, L. Lumata, The effect of glassing solvent deuteration and $Gd^{3+}$ doping on $^{13}$C DNP at 5 T, RSC Adv. 6 (2016) 38855–38860, https://doi.org/10.1039/C6RA02864K.

[60] F. Kurdzesau, B. van den Brandt, A. Comment, P. Hautle, S. Jannin, J.J. van der Klink, J.A. Konter, Dynamic nuclear polarization of small labelled molecules in frozen water–alcohol solutions, J. Phys. D Appl. Phys. 41 (2008), https://doi.org/10.1088/0022-3727/41/15/155506.

[61] B. Vuichoud, J. Milani, A. Bornet, R. Melzi, S. Jannin, G. Bodenhausen, Hyperpolarization of deuterated metabolites via remote cross-polarization and dissolution dynamic nuclear polarization, J. Phys. Chem. B. 118 (2014) 1411–1415, https://doi.org/10.1021/jp4118776.

[62] B. Van Den Brandt, E.I. Bunyatova, P. Hautle, J.A. Konter, DNP with the free radicals deuterated TEMPO and deuterated oxo-TEMPO, Nucl. Instruments Methods Phys. Res. Sect. A Accel. Spectrometers, Detect. Assoc. Equip. 526 (2004) 53–55, https://doi.org/10.3872/j.issn.1007-385X.2010.06.007.